

Superconducting Quantum Interference Device: The Most Sensitive Detector of Magnetic Flux

Hong-Chang Yang^{1,3}, Jau-Han Chen¹, Shu-Yun Wang¹, Chin-Hao Chen¹, Jen-Tzong Jeng¹, Ji-Cheng Chen¹, Chiu-Hsien Wu¹, Shu-Hsien Liao² and Heng-Er Horng^{2,3}

¹*Department of Physics
National Taiwan University
Taipei, Taiwan 106, R.O.C.
E-mail: hcyang@phys.ntu.edu.tw*

²*Department of Physics
National Taiwan Normal University
Taipei, Taiwan 117, R.O.C.*

³*Institute of Opto-Electronics
National Taiwan Normal University
Taipei, Taiwan 117, R.O.C.*

Abstract

SQUIDs are the most sensitive devices in detecting the magnetic flux. The devices have been used to detect small magnetic field, current, voltage, inductance and magnetic susceptibility etc. In this work, we reported studies and applications of high- T_c $YBa_2Cu_3O_y$ SQUIDs. Two main techniques of depositing YBCO thin films are described; the characteristic of thin film and high- T_c SQUID are addressed. In magnetocardiography (MCG) application, we set up an electronic SQUID gradiometer system to optimize the environmental noises. The MCG measurements are performed in magnetically unshielded environments. In the SQUID NDE with the SQUID magnetometer and gradiometer were used to detect the buried flaws. The phase-depth relation of the buried flaw shows linear dependence. It was found that the phase-depth relation is useful to evaluate the depth of the buried flaws. In the scanning SQUID microscopy, the SQUID probe is used to detect the circuits using the lock-in detection technique. We successfully demonstrate that we can image the electrical circuits with the SQUID probe with samples at room temperature.

Key Words: SQUID, Electronic SQUID Gradiometer, Magnetocardiography, Nondestructive Evaluation, SQUID Microscopy.

1. Introduction

The direct current superconducting quantum interference device (dc SQUID) consists of two Josephson junctions connected in parallel. When the SQUID is biased with a current greater than the critical current, the voltage across the SQUID is modulated with the flux threading the SQUID at a period of one flux

quantum, $\Phi_0 \equiv h/2e$ shown in Figure 1. Therefore, the SQUID is a flux-to-voltage transducer. This special flux-to-voltage characteristic has enabled us to use the device to detect small magnetic field, current, voltage, inductance and magnetic susceptibility etc.

SQUIDs are the most sensitive devices in detecting the magnetic flux. Low- T_c SQUID has been used in a wide range of applications,

including biomagnetism [1-2], susceptometers [3], nondestructive evaluation [4], geophysics [5], scanning SQUID microscope [7], and nuclear magnetic resonance [7] etc. Low- T_c SQUIDs are developed for these applications. In this work we will focus on high- T_c $\text{YBa}_2\text{Cu}_3\text{O}_y$ (YBCO) dc SQUIDs [8]; starting from the growth of YBCO thin film, characteristics to SQUID applications.

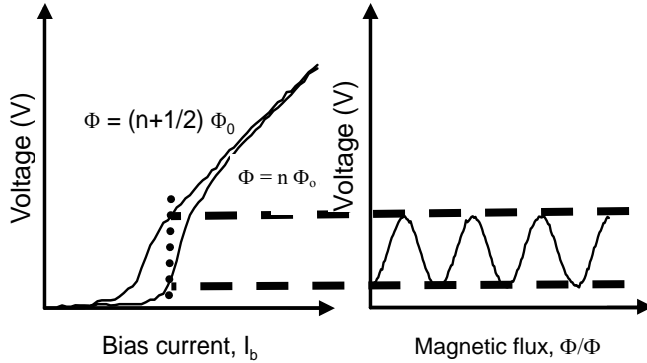


Figure 1. I-V and V- Φ curves of SQUID. The voltage across the SQUID is modulated with the flux threading the SQUID at a period of one flux quantum, $\Phi_0 \equiv h/2e$.

2. Growth of YBCO Thin Films

Among the many different techniques used to prepare YBCO films, the most widely used techniques are pulse laser deposition and sputtering. We have developed both the off-axis pulse laser deposition and the off-axis magnetron sputtering technique to prepare smooth YBCO films [9] with excellent electrical properties. During magnetron sputtering process, a mixture of oxygen and argon (7:3) was kept at 300 mTorr and the temperature of the substrate was kept at 700 °C. After the deposition, oxygen of 650 mTorr was introduced to the sample chamber. The sample was cooled down to 600 °C at a rate of 5 °C per minute and was kept at 600 °C for an hour. After that step, the sample was then cooled down to 25 °C at a rate of 5 °C per minute. With the pulsed laser deposition [10], the oxygen partial pressure was kept at 400 mTorr and the substrate temperature was maintained at about 650 °C. The ArF excimer laser was operated at repetition rate of 10 Hz and produces 20 ns pulses with an energy density of about 1.5 J/cm² on the target. The spot size on the target is about 0.8 mm x 2.5 mm. After depositing the films, the chamber is filled with about 600 Torr

of oxygen, and thermally annealed for 5 minutes. The sample was cooled at a rate of about 20 °C/min to 400 °C and then the heater was turn off. The as-deposited YBCO films are superconducting without any post-annealing at high temperatures. The root mean square roughness of the YBCO films was varied from 50 Å to 150 Å depending on the growth conditions. The substrates for thin film deposition are rotating during the deposition. The critical current densities are higher than 10⁶ A/cm² at 77 K for films prepared from the sputtering or the pulsed laser deposition. To deposit Au layer for electrical contacts, one can use thermal evaporation or sputtering with the substrates at 295 K. We can anneal the samples at 400-500 °C to achieve a low contact resistance lower than 10⁻⁶ Ωcm.

3. Fabrication of SQUID Devices

Types of high- T_c Josephson junctions include bicrystal grain-boundary junctions, step-edge grain-boundary junctions, ramp-edge step-edge junctions, step-edge SNS junctions etc. In this section we briefly show how we can fabricate the high quality step-edge substrates and SQUIDs.

We have developed the technology to fabricate smooth YBCO step-edge substrate. Figure 2 shows the geometry of the Ar⁺ ion milling system we set up to fabricate the step-edge substrates and the SQUIDs devices [11]. The substrate can be rotated so that we can orient the substrate to arbitrary direction with respect to the direction of the incident Ar⁺ ion beam. With this system we prepare smooth step-edge SrTiO₃ or MgO substrates and the angle of the substrates are varied from low angles to high angles.

Conventional photomasking followed by Ar⁺ ion milling is the most commonly used method to fabricate the SQUIDs. Figure 3 showed the YBCO bare SQUID fabricated onto step-edge MgO(100)m substrate. To minimize the damage to the YBCO film, the energy of the incident Ar⁺ ion beam was kept lower than 500 eV. To reduce the deterioration of the quality of the YBCO film, it is also important to cool the sample either with cooled water or liquid nitrogen. To fabricate devices with submicrometer dimensions, it is preferable to cool the sample with liquid nitrogen.

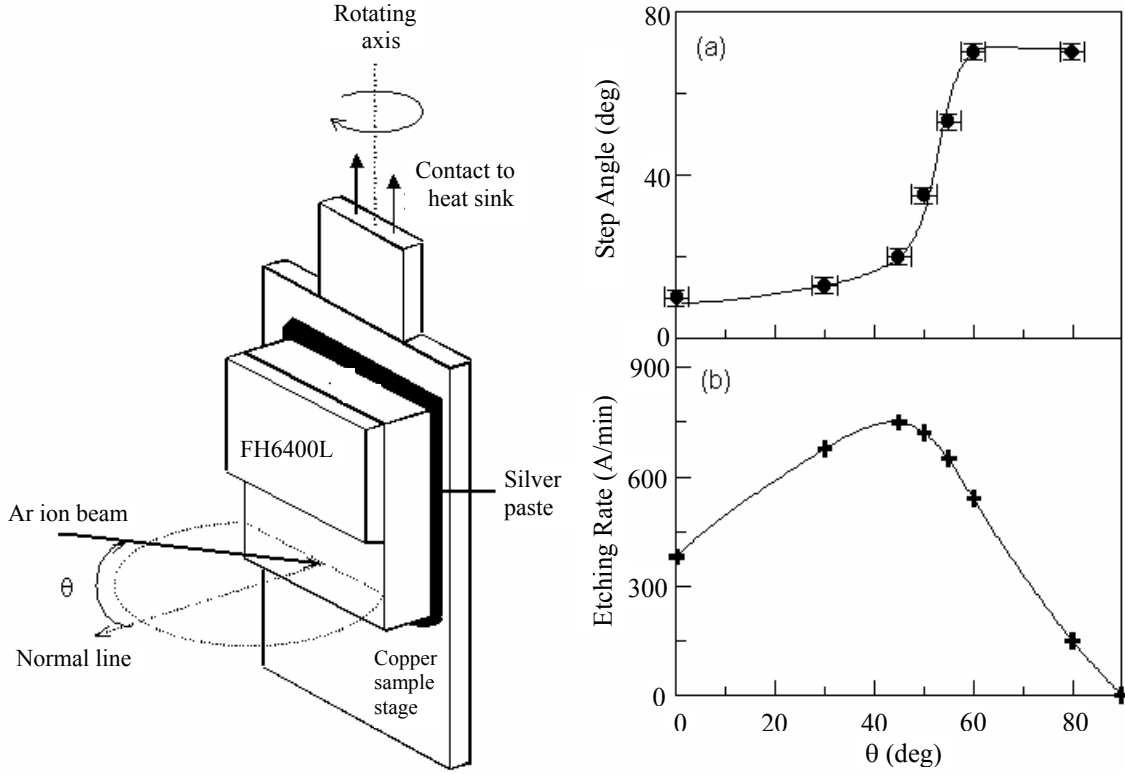


Figure 2. (a) The geometry of the Ar⁺ ion milling system; (b) step angle and; (c) etching rate as a function of θ . θ is the angle the direction of the Ar⁺ ion beam made with respect to the normal of the substrate.

Geometrical configuration of step-edge bare SQUID

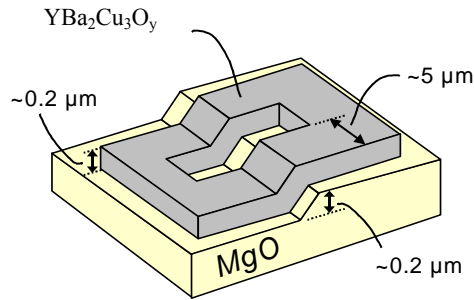


Figure 3. The YBCO bare SQUID fabricated onto the step-edge MgO(100) substrate

4. Parameters for dc SQUID

Two parameters are important in determining the characteristics of SQUID. One is the critical current modulation parameter β_L , $\beta_L = 2LI_c/\Phi_0$. The operating condition is $\beta_L \approx 1$ for optimizing the SQUID resolution [12]. The other parameter is Stewart-McCumber parameter (or hysteresis parameter) β_C [13,14]. The Stewart-McCumber or hysteresis parameter, β_C

$$\beta_c \equiv \frac{2\pi I_c R_n^2 C}{\Phi_0} \quad (1)$$

which is a measure of the damping of the Josephson junction. Generally speaking, β_C must be kept at a value which less than one to let the I - V curve to be non-hysteretic.

The thermal noise affects on the performance of SQUIDs. It tends to round off at the corner of the I - V curve. The noise can be characterized as the

noise parameter Γ given by

$$\Gamma = \frac{2\pi k_B T}{I_c \Phi_0} \quad (2)$$

To avoid the magnetic flux to jump around the SQUID loop, one restrict the flux energy per flux quantum, $\Phi_0^2/2L_s$, to be larger than the thermal energy $\frac{\Phi_0^2}{2L_s} \geq 2\pi k_B T$ (3)

Then the inductance L_s of SQUID should be kept at a value less than 320 pH. For high- T_c SQUIDS a good performance is usually designed with inductance in the range of 50 pH < $L < 100$ pH.

5. Flux Power Spectral Density and Modulation Voltage of dc SQUID

An important figure of merit for dc SQUIDS is the noise energy per unit bandwidth, usually referred to as the energy resolution of the SQUID. The energy resolution is defined as

$$\varepsilon(f) = \frac{S_\Phi(f)}{2L_s} \quad (4)$$

in which the flux power spectral density $S_\Phi(f)$ is given by

$$S_\Phi(f) = \frac{S_V(f)}{\left(\frac{\partial V}{\partial \Phi}\right)^2} \quad (5)$$

It has been shown that the transfer function at the optimal point of operation of the dc SQUID is given by [15]

$$\frac{\partial V}{\partial \Phi} = \frac{7}{\pi} \frac{I_c R_n}{(1 + \beta_L) \Phi_0} \left(1 - 3.57 \frac{\sqrt{k_B T L}}{\Phi_0}\right) \quad (6)$$

in which T is the operating temperature of the SQUID. The term in the brackets accounts for the effect of thermal noise. The thermal noise becomes significant for large inductances and at high temperatures. We can express the modulation voltage, ΔV as following:

$$\Delta V = \frac{7}{\pi^2} \frac{I_c R_n}{(1 + \beta_L)} \left(1 - 3.57 \frac{\sqrt{k_B T L}}{\Phi_0}\right) \quad (7)$$

where $\frac{\partial V}{\partial \Phi} \cong \pi \frac{\Delta V}{\Phi_0}$

Figure 4 shows the modulation voltage, ΔV ,

versus SQUID inductance under different I_c 's and the same R_n . The results of the simulation indicate that SQUID with higher $I_c R_n$ products result in a larger modulation voltage.

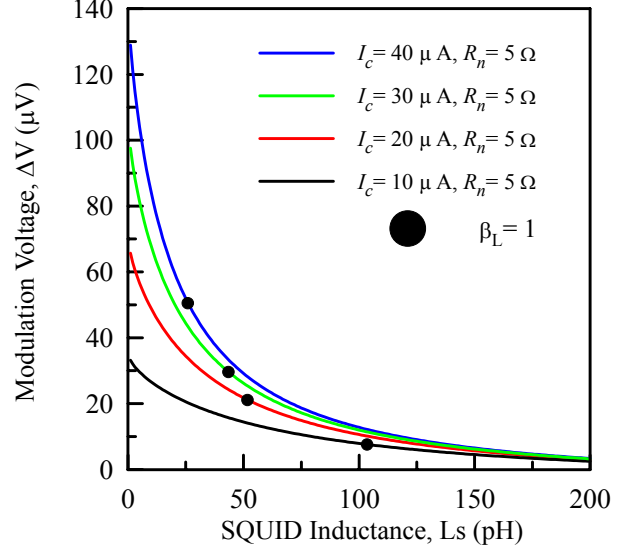


Figure 4. The modulation voltage, ΔV , as a function of the SQUID inductance for different I_c 's and the same R_n

6. Directly Coupled SQUID Magnetometer

The magnetic field sensitivity of bare SQUID is limited by its area. To increase the sensitivity one can couple the SQUID with the pickup coil to form the directly coupled SQUID magnetometer shown in Figure 5. The magnetic signal detected from the pickup loop is coupled to the SQUID via an induced current injected into the SQUID loop. The advantage of a directly coupled SQUID magnetometer is that only single fabrication process is required for the entire magnetometer. Therefore it is simple to fabricate the devices and can have high yield in the device fabrication.

Directly Coupled dc SQUID Magnetometer

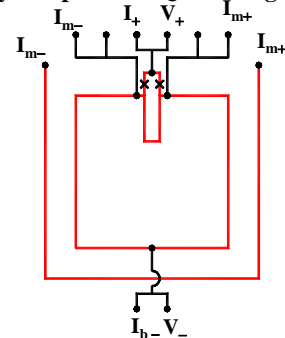


Figure 5. The geometry of the directly coupled SQUID magnetometer, also shown current, voltage, and modulation leads of SQUID

The effective flux capture area of a directly coupled magnetometer is given by [16]

$$A_{eff} = A_s + kL_s \frac{A_p}{L_p} \quad (12)$$

where A_s is the effective area of the bare SQUID, k is a constant which describes the coupling efficiency, A_p and L_p are the area and inductance of the pickup loop, respectively. To maximize A_{eff} , we must maximize the ratio of kA_p/L_p and use the largest SQUID inductance L_s permitted by other constraints.

In good quality directly coupled high- T_c magnetometers the white noise is about $10 \mu\Phi_0/\sqrt{\text{Hz}}$. Furthermore, some results show that the white noise can be lowered to several $\mu\Phi_0/\sqrt{\text{Hz}}$. Now, the magnetometers show magnetic field noise of $S_B^{1/2} = 10\text{-}50 \text{ fT}/\text{Hz}^{1/2}$ in the white noise region at 77 K [17-19].

The relevant figure of merit for a magnetometer is the root mean square magnetic field noise, $S_B^{1/2}(f) = S_\Phi^{1/2}(f)/A_{eff}$. Thus, to reduce the magnetic field noise one needs to minimize the flux noise and maximize the effective area.

Figure 6 shows representative $V-\Phi$ characteristic for a step-edge YBCO SQUID grown on a step-edge MgO substrate at 77 K. The I-V curve of the SQUID shows the resistively shunted junction behavior. As the bias current is increased, the amplitude of the voltage increases smoothly to a maximum and then decreases. The SQUID is normally operated at the bias current that gives the maximum value of $\partial V/\partial\Phi$.

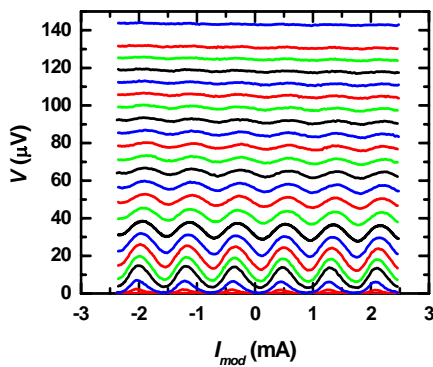


Figure 6. $V-\Phi$ characteristic for an step-edge YBCO SQUID on MgO substrate at 77 K

In Figure 7 we show the $V-\Phi$ curves of a directly coupled SQUID magnetometer at different temperatures. The critical current of SQUID is 12

μA , the normal state resistance is 5.2Ω and the product of the $I_c R_n$ is $62.4 \mu\text{V}$ at 77 K. The experimental modulation voltage is $6 \mu\text{V}$, which is a bit smaller than the theoretical estimated value from Eq. (7).

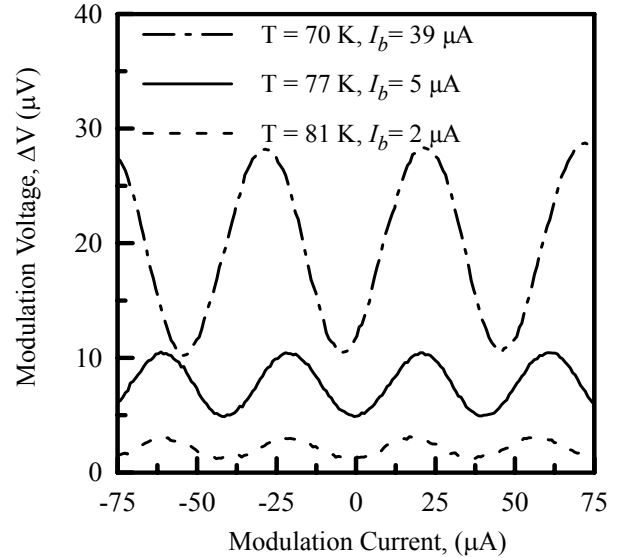


Figure 7. $V-\Phi$ curves of a directly coupled SQUID magnetometer at different temperatures

Dual-channel dc SQUID magnetometer layouts on a $10 \text{ mm} \times 10 \text{ mm}$ SrTiO_3 bicrystal substrate are shown in Figure 8. The square pick-up loop has an outer side length 4 mm and an inner side length 1 mm which is surrounded by an integrated modulation coil of The distance between the two integrated modulation coils of width $100 \mu\text{m}$. The SQUID body with a hole area of $75 \mu\text{m} \times 4 \mu\text{m}$. The junction width is $2 \mu\text{m}$. The flux noise of this SQUID magnetometer in dc and ac bias is shown in Figure 9. The magnetic field sensitivity of the SQUID is $150 \text{ fT}/\text{Hz}^{1/2}$ at 1 kHz . The white noise level is comparable to the current status of the SQUID magnetometers for SQUID with a size of $5 \times 5 \text{ mm}^2$. The low frequency $1/f$ noise was observed.

There are two main separate sources of $1/f$ noises. One is from the motion of vortices. The other is from the fluctuation of critical current in junctions. Resistance fluctuation can contribute the $1/f$ noises. However, at low voltages where the SQUID are operated, the critical current fluctuation dominates the resistance fluctuation. The $1/f$ noise due to the critical fluctuation can be removed with the technique of the ac bias reversal technique [8]. Due to the low frequency noise cannot be reduced with the ac bias reversal technique, we attribute the low frequency $1/f$ noise mainly to the flux motion in this sample.

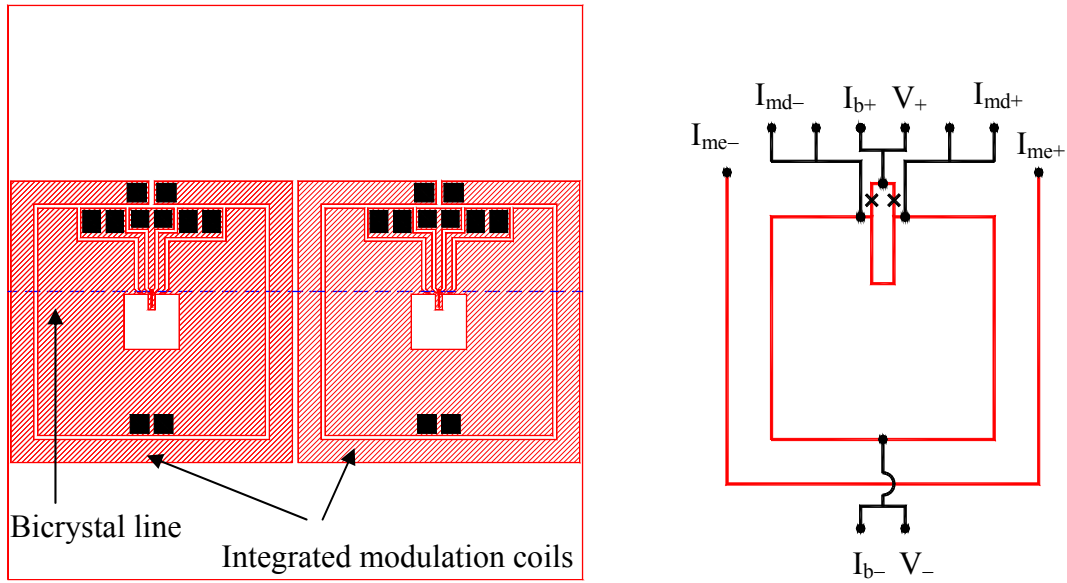


Figure 8. Schematic diagram of the dual-channel dc SQUID magnetometers on a 10 mm x 10 mm SrTiO₃ bicrystal substrate with integrated modulation coils (not drawn to scale). The right side is the directly coupled SQUID magnetometer.

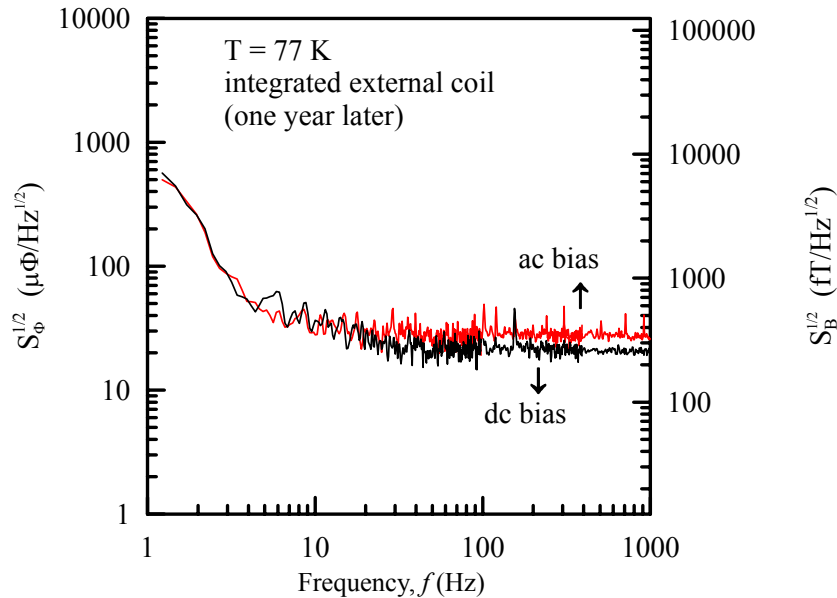


Figure 9. Flux noise of the SQUID magnetometer. The magnetic field sensitivity of the SQUID is 150 fT/Hz^{1/2} at 1 kHz.

7. SQUID Applications

As the sensitivity of high- T_c SQUID has progressively improved, the range of applications has grown rapidly. Currently, the most interest is focused on magnetocardiography, and to some extent in NDE, SQUID microscope, and other applications [20].

7.1 Biomagnetism

A major requirement for biomagnetic measurements is high magnetic field-sensitivity

at frequencies down to 1 Hz. Low- T_c SQUID has already met this requirement. The niobium based SQUID magnetometer has achieved a sensitivity of a few fTHz^{-1/2}. The $1/f$ noise in high- T_c SQUIDs is an issue and to reduce the low frequency noise of the high- T_c SQUID has been a major challenge.

Biomagnetism refers generally to the measurement of magnetic fields produced by any living organism. These biomagnetic fields range from several tens of picotesla from human heart down to a several hundreds of femtotesla from

human brain. Demonstrations of the MCG have been reported in shielded, moderate shielded or unshielded environments [21-23].

To measure the MCG in unshielded environments is more challenging because the MCG signal is quite small compared with the environmental noises. To get rid off the environmental noise, we set up an off-axis 2nd order SQUID magnetocardiography (MCG) system in unshielded environments and developed the fast Fourier technique to reduce the noise of the SQUID MCG system. The detailed description of the noise reduction and the Fourier transform technique was reported in references [24]. Figure 10 shows the configuration of the MCG system we have developed. Three rf SQUIDs are arranged inside the liquid nitrogen dewar with an off-axis configuration. The SQUIDs are controlled with the SQUID electronics. The output of the SQUID is fed to the analog compensation electronics to form 1st order and 2nd order gradiometer. The output of the 2nd gradiometer is further filtered with the notch filter and the low frequency filter. With optimum parameters in compensation electronics and filtering, the peak-to-peak value of the background field can be reduced from about 60 nT to about 25 pT. The noise level at 10 Hz is $\sim 0.1 \text{ nT/Hz}^{1/2}$ for the magnetometer in unshielded environments and this noise is reduced to $1.5 \text{ pT/Hz}^{1/2}$ for the 2nd-order gradiometer. This noise is much lower than the typical MCG signal of human heart. Therefore, we can perform the MCG of human in unshielded environments with averaging. Figure 11 shows the averaged MCG signal over the chest of human for 25 different measurement sites. The rate of heartbeat of our subject is about 72 beats/min. The measurement of each position was taken 90 seconds for recording more data to average. Each position is spaced by 4 cm. The total time display in the figure is 800 ms, about the time between two heartbeats. The time, which the averaging data displayed, is chosen to be about the period of single heartbeat to prevent losing any information. Note that at the instance about 0.3 sec, the upper right signals display positive amplitudes whereas the lower left signals display negative amplitudes. The T wave in the upper right of Figure 11 also display positive amplitudes and in the lower left of the figure display negative amplitudes, similar as that at the instance of 0.3 sec.

Second-order SQUID Gradiometer MCG System

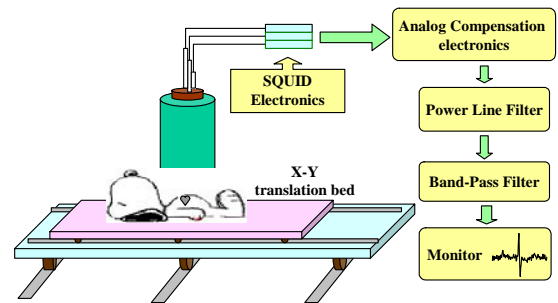


Figure 10. Configuration of the 2nd order SQUID gradiometer system for the MCG



Figure 11. Averaged MCG signal over a scanned area of $120 \times 20 \text{ cm}^2$

7.2 Nondestructive Evaluation

Nondestructive evaluation (NDE) is the noninvasive examination of flaws of materials. These are varieties of techniques used in NDE, for instance, acoustic, thermal, and electromagnetic methods. These methods are often not adequate for detecting flaws at an early stage because of the lack of the space and the depth resolution. One important application of high- T_c SQUID is to replace the induction coil in the eddy current imaging by the SQUID sensor. In this method one applies an alternating magnetic field produced by the drive coil

and lock-in detected the magnetic fields induced the eddy current around the flaws. Since the eddy current over the skin depth, which is inversely proportional to the square root of the frequency, deep flaws require corresponding low frequencies. The flat response of SQUIDs shows a distinct advantage over the response of detection coils, which fall off with decreasing frequency. Furthermore, high- T_c SQUIDs are preferable over the low- T_c SQUID because the associated lighter dewar and the easy handling of the nitrogen liquid.

The NDE detection of flaws using high- T_c SQUIDs has been reported by several groups [25-30]. Both magnetometers or gradiometers have been used. We have also done works on SQUID NDE. Jeng et al. [28-30] developed high- T_c NDE nondestructive evaluation (NDE) system to detect flaws in aluminum sheets. The NDE systems were in the unshielded environment [29,30]. We also simulated the magnetic field produced by the eddy current around the defect and the results are consistent with the simulation [31,32]. Recently, we investigated flaws with NDE systems with an integrated planar gradiometer [24]. Figure 12 shows the schematics of the NDE system using the planar gradiometer. The system was developed to detect buried flaws with the differential phase technique for the magnetic field of the eddy current from the defects in aluminum plates. The results of SQUID NDE with the integrated planar SQUID gradiometer were compared with those derived from an axial electronic SQUID gradiometer. The phase-depth relations of the buried flaw show linear dependences as shown in Figure 13. The phase depth relation can be useful to evaluate the depth of the buried flaws. The results for both systems are consistent. Overall, the SQUID NDE system with the planar gradiometer is relatively simple and practical in unshielded environments.

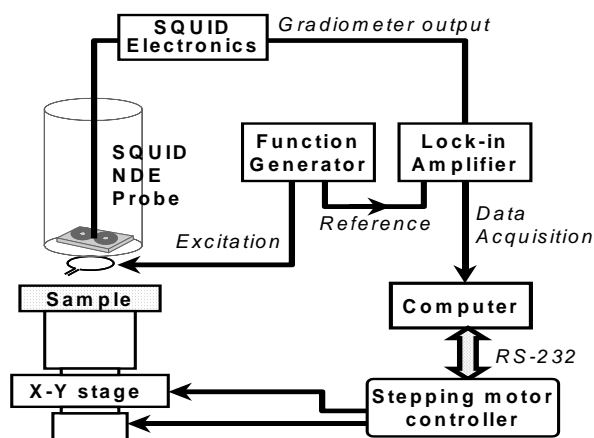


Figure 12. Schematics of the planar NDE system.

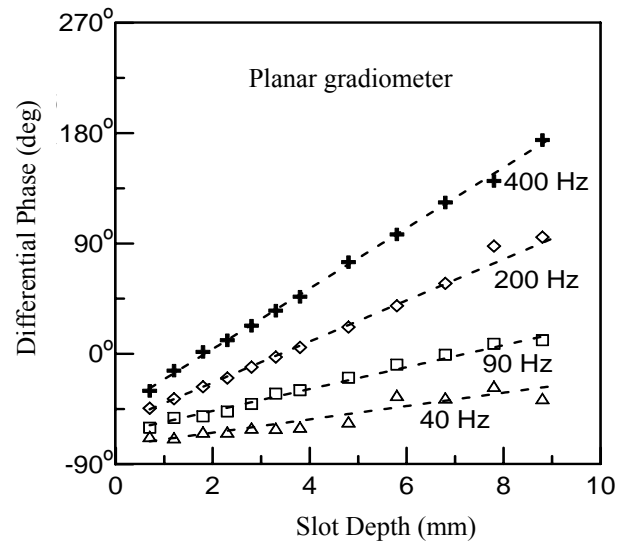


Figure 13. The phase-depth relation of the buried flaw

7.3 SQUID Scanning SQUID (SSM) System

Magnetic microscope based on the SQUIDs has been developed to image magnetic fields, in which the sample is either at low temperature or at room temperature. Most cases the samples are scanned across the SQUID. The best resolution of the scanning SQUID microscope with cold sample is about $5 \mu\text{m}$ while those with room temperature sample the spatial resolution is $50 \mu\text{m}$. A magnetic tip has been used [34] to focus the flux into the sample to achieve a higher spatial resolution. The potential of the microscope for biology is intriguing. One novel example is the immunoassay. Here one labels an antibody with a tiny magnetic particle and then bind it to the antigen. The binding of the antibody and the antigen is immobile particles. One can detect the particles with magnetic relaxation, remanent magnetization, or susceptibility.

For the future SQUID applications, we developed the SQUID SSM system. We used the pulse laser deposition (PLD) to grow YBCO film and then fabricate SQUID. The SQUID we made is a bare SQUID with a hole area of $50 \times 50 \mu\text{m}^2$ and a junction width of $5 \mu\text{m}$. The noise of the SQUID is $12 \text{ pT/Hz}^{1/2}$ at 1 kHz in shielded environments. The V_{pp} of the SQUID is $6 \mu\text{V}$ and the effective area is $5.8 \times 10^{-7} \text{ m}^2$.

The SQUID SSM system was first used to examine the electrical circuits. The circuit is the grid like pattern shown on the left-hand side. The size of each grid is $4 \text{ mm} \times 4 \text{ mm}$ and the line width is 1 mm shown in Figure 14. The distance between the SQUID and the circuit is 1 mm . The

magnetic field pattern of the tested circuit is generated from the function generator and the magnetic field is then lock-in detected. The magnetic field image is shown in the false color. The dark and bright parts represent the opposite directions of the magnetic field. The boundary between the dark and the bright area corresponds to the circuit. The magnetic field image clearly shows the pattern of the circuit. Using the Biot-Savart law, we simulate the magnetic field distribution of the circuit pattern. Our results of the simulation shown in Figure 15(b) are consistent to the scanned imaging. The SSM for detecting the flaws in electrical circuit can be found in reference [35]. The present success of the SSM paves the way for our future research on immunoassay using SQUIDs.

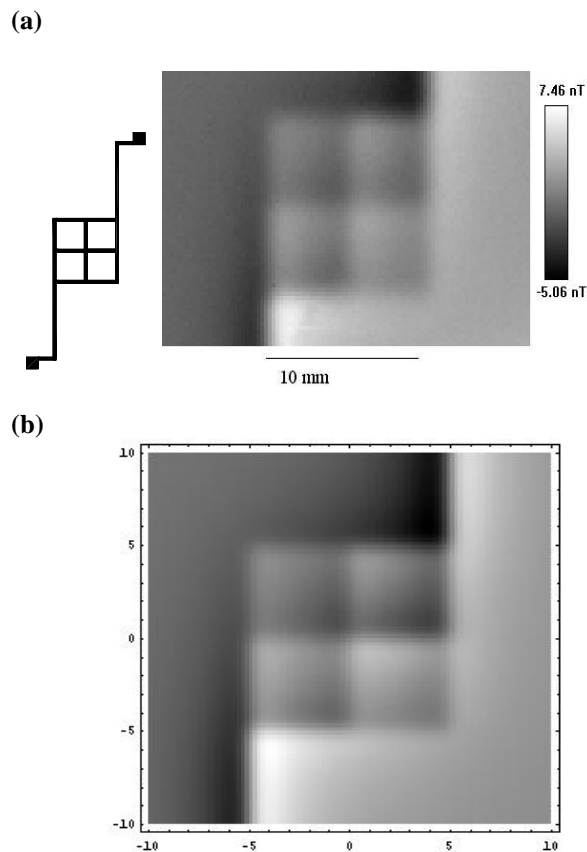


Figure 14. (a) Geometry of the grid along with the scanned image; (b) the image from the simulation

8. Conclusion

Though the efforts on high- T_c SQUID over the decade, we now understand better the device physics. The reduction of the low frequency $1/f$ noise is improved for high- T_c SQUID. The progress of high- T_c SQUID shows that it is

adequate for many practical applications. Indeed, one important application of biomagnetism is the magnetocardiography. The clinical results on MCG are encouraging and clinical efforts on large number of patients have to be done. One might hope that the high- T_c MCG system will become more wide spread modality over the next few years, for instance, in the assessment of damage to heart muscle following a cardiac infarction or to locating the sources of certain kind of arrhythmia. The MCG are largest potential for the high- T_c SQUID in biomagnetic applications. Other applications in NDE and SSM can also be promising in the future demands. More works both in basic and application are needed to achieve these goals.

Acknowledgment

The authors thank the grants of the National Science Council of the R.O.C. and the program of the Ministry of Education for promoting the academic excellence.

References

- [1] Pizzella, V.; Penna, S. D.; Gratta, C. D.; Romani, G. L. *Supercond. Sci. Technol.* **2001**, *14*, R97.
- [2] Vrba, J. *Physica C*. **2002**, *368*, 1.
- [3] The SQUID Susceptometer from Quantum Design Inc. is the commercial product using low T_c SQUID.
- [4] Jenks, W. G.; Sadeghi, S. S. H.; Wikswo Jr, J. *P. J. Phys. D. Appl. Phys.* **1997**, *30*, 293.
- [5] Clarke, J. *IEEE Trans. Magn.* **1983**, *MAG-19*, 288.
- [6] Tsuei, C. C.; Kirtley, J. R.; *Physica C*, **2002**, *367*, 1.
- [7] Greenberg, Ya. S.; *Rev. Mod. Phys.* **1998**, *70*, 175.
- [8] Koelle, D.; Kleiner, R.; Ludwig, F.; Danster, D.; Clarke, J. *Rev. Mod. Phys.* **1999**, *71*, 631.
- [9] Wang, L. M.; Yu, H. W.; Yang, H. C.; Horng, H. E. *Physica C*. **1996**, *256*, 57.
- [10] Chen, K.-L.; Chen, J.-H.; Yang, H.-C.; *Physics C*. **2003**, in press.
- [11] Yang, S. Y.; Chen, C.-H.; Jeng, J. T.; Horng, H. E.; Yang, H. C. *Inst. Phys. Conf. Seri.* **1999**, *167*, 189.
- [12] Tesche, C. D.; Clarke, J. *J. Low Temp. Phys.* **1977**, *29*, 301.
- [13] Stewart, W. C. *Appl. Phys. Lett.*, **1968**, *12*, 277.
- [14] McCumber, D. E. *J. Appl. Phys.* **1968**, *39*, 3113.

- [15] Enpuku, K.; Shimomura, Y.; Kisu, T. *J. Appl. Phys.* **1993**, *73*, 7929.
- [16] Clarke, J.; Danster, E.; Kleiner, R.; Koelle, D.; Miklich, A. H.; Ludwig, F. *Chin. J. Phys.* **1996**, *34*, 352.
- [17] Cantor, R.; Lee, L. P.; Teepe, M.; Vinetskiy, V.; Longo, J. *IEEE Trans. Appl. Supercond.* **1995**, *5*, 2927.
- [18] Lee, L. P.; Longo, J.; Vinetskiy, V.; Cantor, R. *Appl. Phys. Lett.* **1995**, *66*, 1539.
- [19] Lee, L. P.; Teepe, M.; Vinetskiy, V.; Cantor, R.; Colclough, M. S. *Appl. Phys. Lett.* **1995**, *66*, 3058.
- [20] See for instance, Matz, H.; Drung, D.; Hartwig, S.; Groß, H.; Kötz, R.; Müller, W.; Vass, A.; Weitschies, W.; Trahms, L.; *Appl. Supercond.* **1998**, *6*, 577.
- [21] Tavrín, Zhang, Y.; Mück, Y.; Braginski, A. I.; Heiden, C. *Appl. Phys. Lett.* **1993**, *62*, 1824. Tavrín, Y.; Zhang, Y.; Wolf, W.; Braginski, A. I.; *Supercond. Sci. Technol.* **1994**, *7*, 265; Tavrín, Y.; Seigel, M.; *Appl. Supercond.* **1998**, *1*, 719.
- [22] Zeng, X. H.; Soltner, H.; Selbig, D.; Bode, M.; Bick, M.; Rüdgers, F.; Schubert, J.; Zander, W.; Zhang, Y.; Bousack, H.; Braginski, A. I. *Meas. Sci. Technol.* **1998**, *9*, 1600.
- [23] Matsuda, M.; Matsuura, T.; Kato, K.; Oyama, H.; Hayashi, A.; Hirano, S.; Kuriki, S.; *IEICE Electron.* **2002**, *E85-C*, 677.
- [24] Yang, H.-C.; Wang, S.-Y.; Chen, C.-H.; Jeng, J.-T.; Chen, J.-H.; Horng, H.-E.; *J. Low Temp. Phys.* **2003**, in press.
- [25] Tavrín, Y.; Krause, M. H.-J.; Wolf, W.; Wolf, V.; Glyantsev, V.; Schubert, J. *Cryogenics.* **1995**, *36*, 83.
- [26] Hohmann, R.; Krause, H. -J.; Soltner, H.; Zhang, Y.; Copetti, C. A.; Bousack, H.; Braginski, A. I. *IEEE Trans. Appl. Supercond.* **1997**, *7*, 2860.
- [27] Kreutzbruck, M. V.; Tröll, J.; Mück, M.; Heiden, C.; Hang, Y. Z. *IEEE Trans. Appl. Supercond.* **1997**, *7*, 3279.
- [28] Jeng, J. T.; Horng, H. E.; Chen, C.-H.; Chen, J. H.; Yang, H. C. *Physica C.* **2000**, *341-348*, 2637.
- [29] Jeng, J. T.; Yang, S. Y.; Horng, H. E.; Yang, H. C. *IEEE Trans. Appl. Supercond.* **2001**, *11*, 1295.
- [30] Jeng, J. T.; Horng, H. E.; Yang, H. C. *Supercond. Sci. Technol.* **2002**, *15*, 416.
- [31] Horng, H. E.; Jeng, J. T.; Yang, H. C.; Chen, J. C. *Physica C.* **2002**, *367*, 298.
- [32] Jeng, J. T.; Horng, H. E.; Yang, H. C.; Chen, J. C.; Chen, J. H. *Physica C.* **2002**, *367*, 298.
- [33] Tavrín, Y.; Siegel, M.; in *Proceedings of the Third European Conference on Appl. Supercon. (EUCAS'97)*, Veldhoven, Ed. H. Rogalla and H. D. A. Blank, **1997**, 719.
- [34] Kötz, D.; Matz, H.; Trahms, L.; Koch, H.; Weitschies, W.; Rheinländer, T.; Semmler, W.; Bunte, T.; *IEEE Trans. Appl. Supercond.* **1997**, *7*, 3678.
- [35] Chen, C.-H., M. S. Thesis, National Taiwan University, June **2002**.

**Manuscript Received: Dec. 20, 2002
and Accepted: Jan. 20, 2003**